Supporting Information

Realizing efficient broadband near-infrared emission and multimode photoluminescence switching via coordination structure modulation in Sb^{3+} doped 0D organic metal chlorides

Shuiyue Yu,[a] Hui Peng,[a*] Qilin Wei,[b] Tongzhou Li,[a] Weiguo Huang,[a] Xuefei He,[a] Zhentao Du,[a] Jialong Zhao,[a] and Bingsuo Zou[a *]

[a]State Key Laboratory of Featured Metal Materials and Life-cycle Safety for Composite Structures, School of Resources, Environments and Materials, Guangxi University, Nanning 530004, China.

[b]School of Chemistry and Chemical Engineering, Shandong University, Jinan 250100, China.

Address correspondence to: penghuimaterial@163.com; zoubs@gxu.edu.cn

Experimental methods

Materials: Manganese chloride ($MnCl_2$, 99%), cadmium dichloride hemipentahydrate ($CdCl_2 \cdot 2.5H2O$), zinc chloride ($ZnCl_2$, 98%), ethyl-triphenylphosphonium chloride ($C_{20}H_{20}PCl$, 98%), antimony trichloride ($SbCl_3$, 99.5%), N, N-dimethylformamide (DMF, 99.8%), ethyl ether (Et_2O, 99.5%), and ethanol (EtOH, 99.5%) were purchased from Macklin reagent.

Synthesis of $(C_{20}H_{20}P)_2SbCl_5 \cdot EtOH$ single crystals (SCs): Typically, 1 mmol $SbCl_3$ and 2 mmol of $C_{20}H_{20}PCl$ were dissolved in 3 mL of EtOH at 100 °C to form transparent solution. Subsequently, the above solution was left to stand at RT for 24 hours, and the bulk transparent crystals could be harvested.

Synthesis of $(C_{20}H_{20}P)_2MCl_4$ (M = Mn, Zn, Cd) and Sb^{3+}-doped $(C_{20}H_{20}P)_2MCl_4$ SCs: $(C_{20}H_{20}P)_2MCl_4$ SCs were synthesized by anti-solvent recrystallization method. Typically, 1-x mmol of MCl_2 and 2 mmol of $C_{20}H_{20}PCl$ were dissolved in 2 mL DMF at 60 °C to form transparent solution. Then, $(C_{20}H_{20}P)_2MCl_4$ SCs can be obtained by diffusing Et_2O into the precursor solution at RT. For synthesizing Sb^{3+}-doped $(C_{20}H_{20}P)_2MCl_4$ SCs, x mmol $SbCl_3$ was used under otherwise identical conditions.

Characterization: The structure information of the samples was determined by single crystal X-ray diffraction (SCXRD, IPDS II-STOE). The morphology was characterized by scanning electron microscopy (SEM) (JEOL, JSM-6360LV). The elemental composition and distribution of the samples were measured by energy-dispersive spectrometry (EDS, Horiba 7021-H). The elemental content of Sb^{3+} was determined inductively coupled plasma optical emission spectrometry (ICP-MS, CONTRAA-700, Analytik Jena Co., GER). The powder XRD (PXRD) patterns were collected by a Bruker D8 discover X-ray diffractometer. X-ray photoelectron spectroscopy (XPS) spectra were collected through Thermo ESCALAB 250XI instrument. Absorption spectra were obtained by UV 3600 plus instrument, where $BaSO_4$ was used as the reference sample. PL and PLE spectra were measured via Edinburgh FS5 spectrometer. Photoluminescence quantum yield (PLQY) data were collected by Edinburgh FLS1000 spectrometer. PL decay lifetimes were also measured by Edinburgh FLS1000 spectrometer. Temperature-dependent PL spectra were measured by HORIBA Fluorolog-QM instrument. Thermal stability was evaluated by Discovery TGA 55 instrument in N_2 atmosphere.

NIR pc-LEDs Fabrication: First, the as-synthesized Sb^{3+}-doped $(C_{20}H_{20}P)_2MCl_4$ powder were uniformly mixed with epoxy resin, and then coated on a 365 nm chip. Subsequently, the EL spectra of the NIR pc-LEDs were collected using Hangzhou Hopoo HPCS6500 instrument.

Table S1. Comparison of the bond lengths of $(C_{20}H_{20}P)_2SbCl_5 \cdot EtOH$ and Sb^{3+}-doped samples in the ground state and excited state.

$(C_{20}H_{20}P)_2SbCl_5 \cdot EtOH$						
	Sb-Cl1(Å)	Sb-Cl2(Å)	Sb-Cl3(Å)	Sb-Cl4(Å)	Sb-Cl5(Å)	Δ*d*
Ground state	2.365	2.619	2.614	2.619	2.614	1.741×10^{-3}
Excited state	2.389	2.677	2.669	2.673	2.644	2.086×10^{-3}
Sb^{3+}-**1**						
	Sb-Cl1(Å)	Sb-Cl2(Å)	Sb-Cl3(Å)	Sb-Cl4(Å)	Δ*d*	
Ground state	2.359	2.353	2.380	2.348	2.738×10^{-5}	
Excited state	2.657	2.613	2.645	2.631	3.878×10^{-5}	
Sb^{3+}-**2**						
	Sb-Cl1(Å)	Sb-Cl2(Å)	Sb-Cl3(Å)	Sb-Cl4(Å)	Δ*d*	
Ground state	2.312	2.340	2.320	2.325	1.793×10^{-5}	
Excited state	2.652	2.615	2.637	2.633	2.531×10^{-5}	
Sb^{3+}-**3**						
	Sb-Cl1(Å)	Sb-Cl2(Å)	Sb-Cl3(Å)	Sb-Cl4(Å)	Δ*d*	
Ground state	2.465	2.497	2.465	2.483	2.872×10^{-5}	
Excited state	2.736	2.711	2.739	2.760	4.045×10^{-5}	

Note: Table S1 shows the bond lengths of $(C_{20}H_{20}P)_2SbCl_5 \cdot EtOH$ and Sb^{3+}-doped samples in the ground state and excited state. The lattice deformation parameters (Δd) in the ground state and excited state for pure Sb(III)-based compound and Sb^{3+}-doped samples were also given in Table S1. Moreover, the excited state lattice distortion degree (η) was calculated via the following equation: (1)

$$\eta = \frac{\Delta d_{ES} - \Delta d_{GS}}{\Delta d_{GS}} \times 100\% \qquad (1)$$

where Δd_{ES} and Δd_{GS} are the lattice deformation parameters (Δd) in the ground state and excited state, respectively. Here, the calculated η of $(C_{20}H_{20}P)_2SbCl_5 \cdot EtOH$, Sb^{3+}-**1**, Sb^{3+}-**2**, and Sb^{3+}-**3** are 19.8%, 41.6%, 41.2%, and 40.8%, respectively. Clearly, the values of η for the Sb^{3+}-doped samples are much larger than pure Sb(III)-based compound, resulting in a larger Stokes shift in Sb^{3+}-doped samples and further enabling us to obtain NIR emission.

Table S2. Detailed crystallographic data for $(C_{20}H_{20}P)_2MnCl_4$, $(C_{20}H_{20}P)_2ZnCl_4$, and $(C_{20}H_{20}P)_2CdCl_4$.

Empirical formula	$(C_{20}H_{20}P)_2MnCl_4$	$(C_{20}H_{20}P)_2ZnCl_4$	$(C_{20}H_{20}P)_2CdCl_4$
Chemical formula	$C_{40}H_{40}Cl_4P_2Mn$	$C_{40}H_{40}Cl_4P_2Zn$	$C_{40}H_{40}Cl_4P_2Cd$
Formula weight	779.40	789.83	836.86
Temperature (K)	297.19	296.15	296.15
Crystal system	monoclinic	monoclinic	monoclinic
Space group	Cc	Cc	Cc
a (Å)	12.223(3)	12.180(2)	12.2339(14)
b (Å)	20.914(4)	20.741(3)	21.044(2)
c (Å)	16.393(3)	16.353(3)	16.5713(19)
α (deg)	90	90	90
β (deg)	110.772(5)	110.644(3)	112.272(2)
γ (deg)	90	90	90
Volume ($Å^3$)	3918.1(14)	3865.9(11)	3948.0(8)
Z	4	4	4
Density (calculated) ($g\cdot cm^{-3}$)	2.039	1.357	1.408
Absorption coefficient (mm^{-1})	3.392	1.022	0.932
Data/restraints/parameters	7697/2/426	7788/2/426	6450/2/426
Goodness of fit on F^2	1.017	0.966	1.059
Final R indexes [I>=2σ (I)]	R_1 = 0.0423, wR_2 = 0.0951	R_1 = 0.0426, wR_2 = 0.0780	R_1 = 0.0313, wR_2 = 0.0741
Final R indexes [all data]	R_1 = 0.0599, wR_2 = 0.1031	R_1 = 0.0662, wR_2 = 0.0874	R_1 = 0.0377, wR_2 = 0.0771

Table S3. Main parameters of processing and refinement of the x%Sb:$(C_{20}H_{20}P)_2MCl_4$ (M = Mn, Zn, Cd) samples.

	Space Group	Cell Parameters (Å) Cell Volume (Å)	R_{wp}, R_p, χ^2
25%Sb^{3+}-doped **1**	*C 1 c 1*	a=12.223(3) b=20.914(4) c= 16.393(3) V=3918.1(14)	4.37%, 3.08%, 1.90
20%Sb^{3+}-doped **2**	*C 1 c 1*	a=12.180(2) b=20.741(3) c=16.353(3) V=3865.9(11)	7.62%, 5.34%, 3.21
20%Sb^{3+}-doped **3**	*C 1 c 1*	a=12.2339(14) b=21.044(2) c=16.5713(19) V=3948.0(8)	7.05%, 4.75%, 3.13

Table S4. Comparison of element concentrations obtained from EDS analysis of x**Sb^{3+}-1**.

Element	5%	10%	15%	20%	25%
Cl (%)	79.45	79.33	79.23	80.14	80.03
Sb (%)	0.93	1.41	2.37	2.73	3.46
Mn (%)	19.62	19.26	18.40	17.13	16.51

Table S5. Comparison of element concentrations obtained from EDS analysis of x**Sb^{3+}-2**.

Element	5%	10%	15%	20%	25%
Cl (%)	79.35	79.53	79.72	79.92	80.16
Sb (%)	0.37	0.62	0.75	0.92	1.21
Zn (%)	20.28	19.85	19.53	19.16	18.63

Table S6. Comparison of element concentrations obtained from EDS analysis of x**Sb^{3+}-3**.

Element	5%	10%	15%	20%	25%
Cl (%)	79.42	79.10	79.52	79.87	80.24
Sb (%)	0.86	1.29	1.59	1.86	2.03
Cd (%)	19.72	19.61	18.89	18.27	17.73

Table S7. The actual element content of Sb^{3+}-doped $(C_{20}H_{20}P)_2MCl_4$ (M = Mn, Zn, Cd) measured by Inductively Coupled Plasma-Atomic Emission Spectrometry (ICP-AES).

Samples	Sb:(M + Sb)	Nominal/mol% (Sb)	Actual/mol% (Sb)
5%Sb^{3+}:$(C_{20}H_{20}P)_2MnCl_4$	5:90	5	0.98
15%Sb^{3+}:$(C_{20}H_{20}P)_2MnCl_4$	15:85	25	2.43
25%Sb^{3+}:$(C_{20}H_{20}P)_2MnCl_4$	25:75	25	3.51
15%Sb^{3+}:$(C_{20}H_{20}P)_2ZnCl_4$	15:85	15	0.77
20%Sb^{3+}:$(C_{20}H_{20}P)_2ZnCl_4$	20:80	20	0.96
25%Sb^{3+}:$(C_{20}H_{20}P)_2ZnCl_4$	25:75	25	1.27
15%Sb^{3+}:$(C_{20}H_{20}P)_2CdCl_4$	15:85	15	1.62
20%Sb^{3+}:$(C_{20}H_{20}P)_2CdCl_4$	20:80	20	1.89
25%Sb^{3+}:$(C_{20}H_{20}P)_2CdCl_4$	25:75	25	2.11

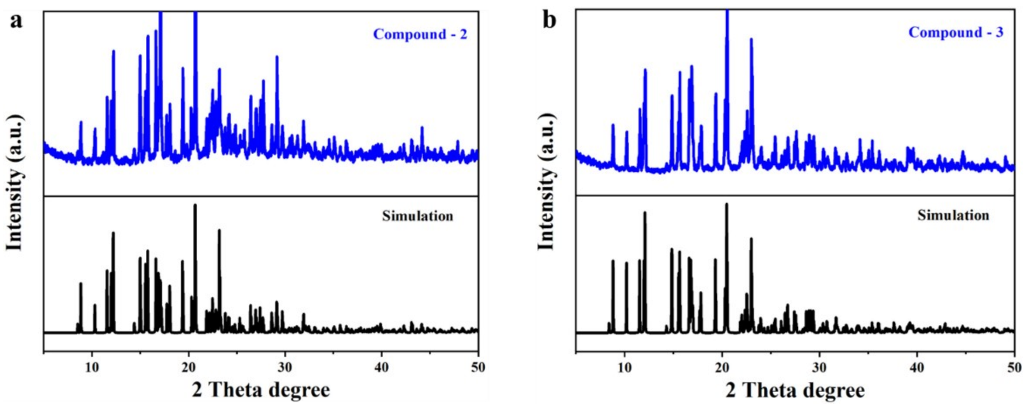

Figure S1. Experimental and calculated PXRD patterns of the as-synthesized compounds, a) Compound **2,** b) and Compound **3**.

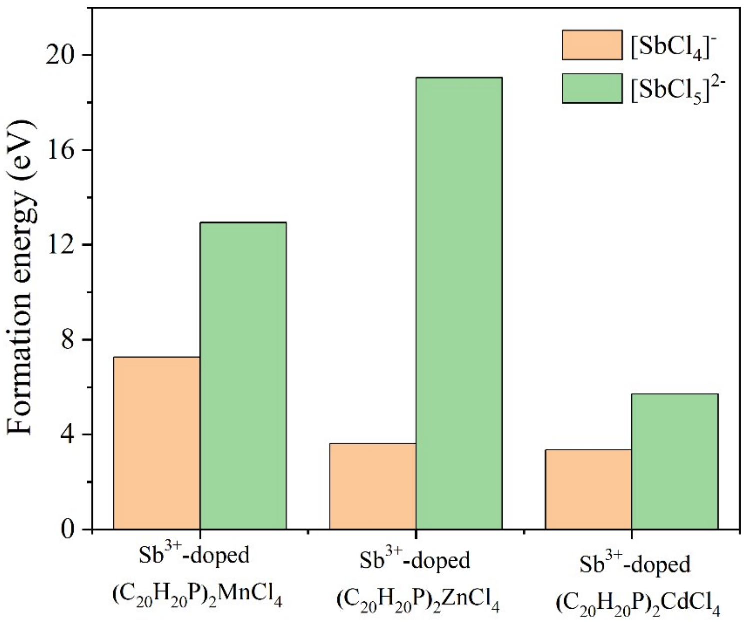

Figure S2. Formation energies of $[SbCl_4]^-$ and $[SbCl_5]^{2-}$ in the host lattice.

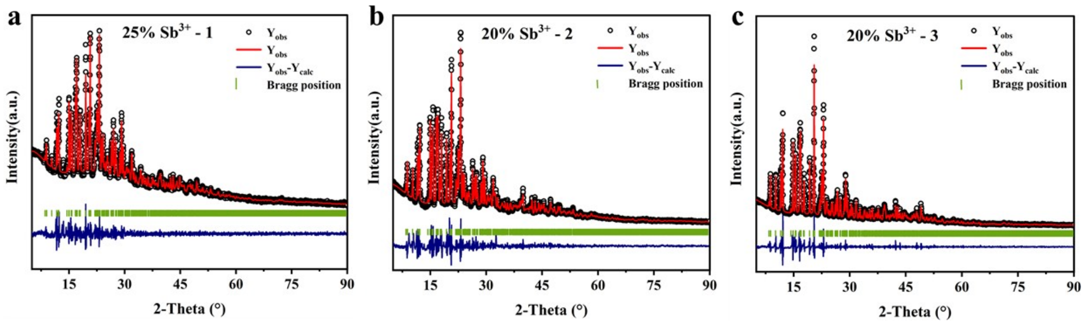

Figure S3. Rietveld refinement plot of PXRD; (a) 25%Sb^{3+}-doped **1**, b) 20%Sb^{3+}-doped **2**, c) 20%Sb^{3+}-doped **3**.

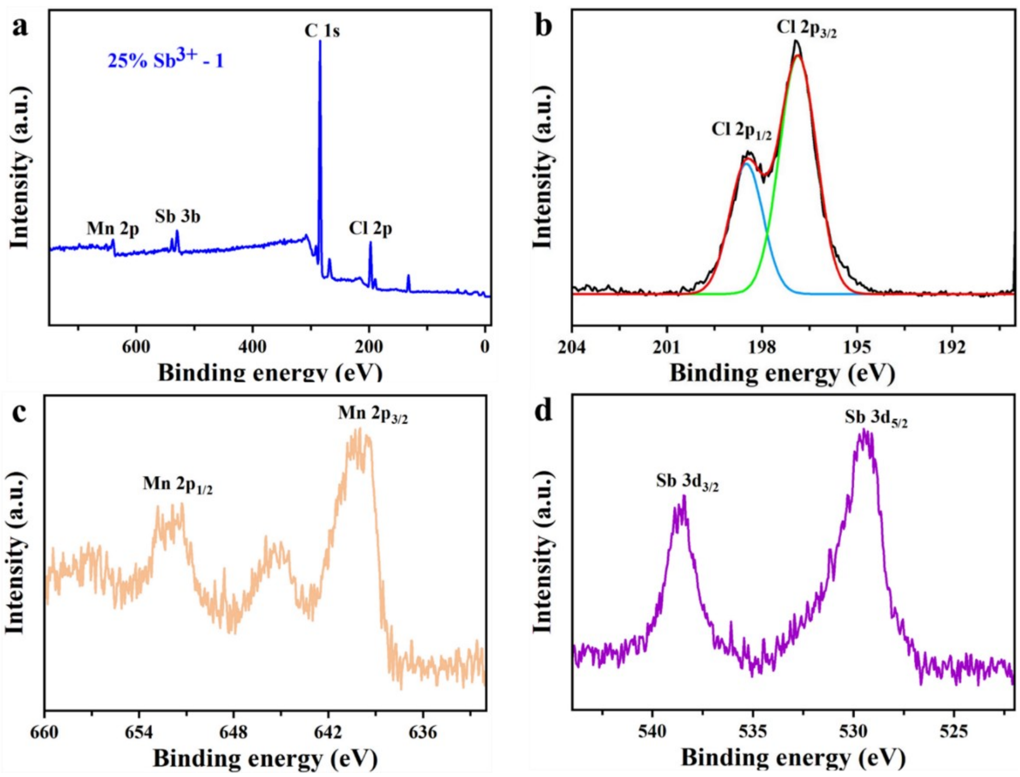

Figure S4. a) XPS spectrum of 25%Sb^{3+}-doped **1** and the corresponding high-resolution XPS spectra of b) Cl 2p, c) Mn 2p, d) and Sb 3d.

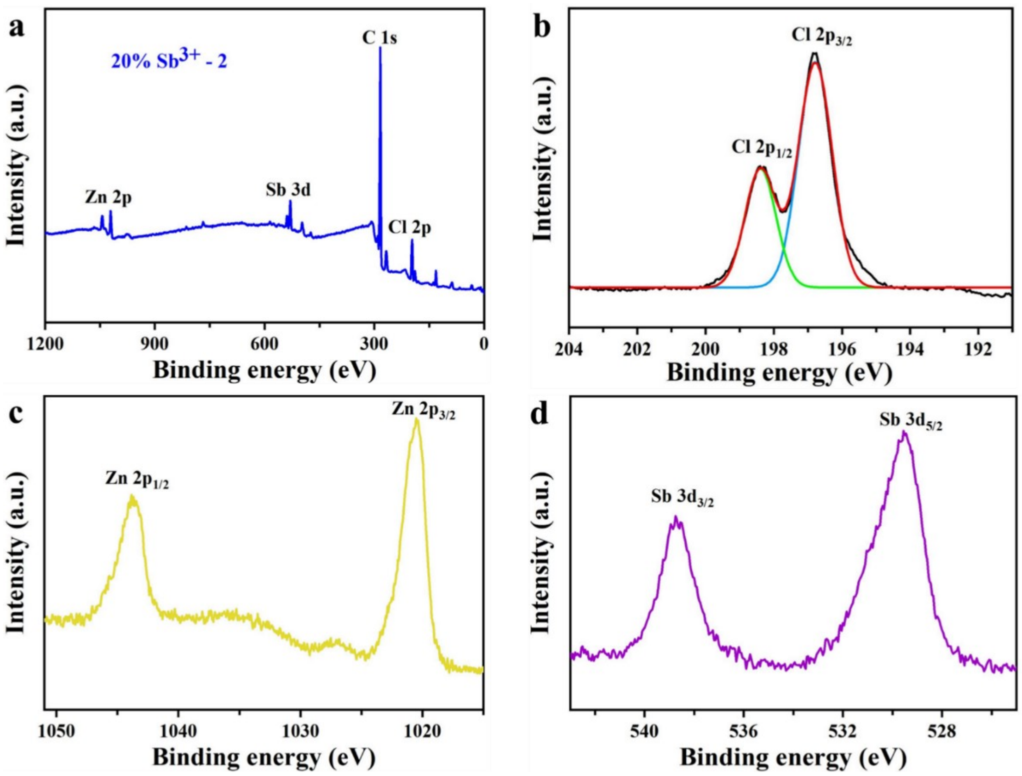

Figure S5. a) XPS spectrum of 20%Sb^{3+}-doped **2** and the corresponding high-resolution XPS spectra of b) Cl 2p, c) Zn 2p, d) and Sb 3d.

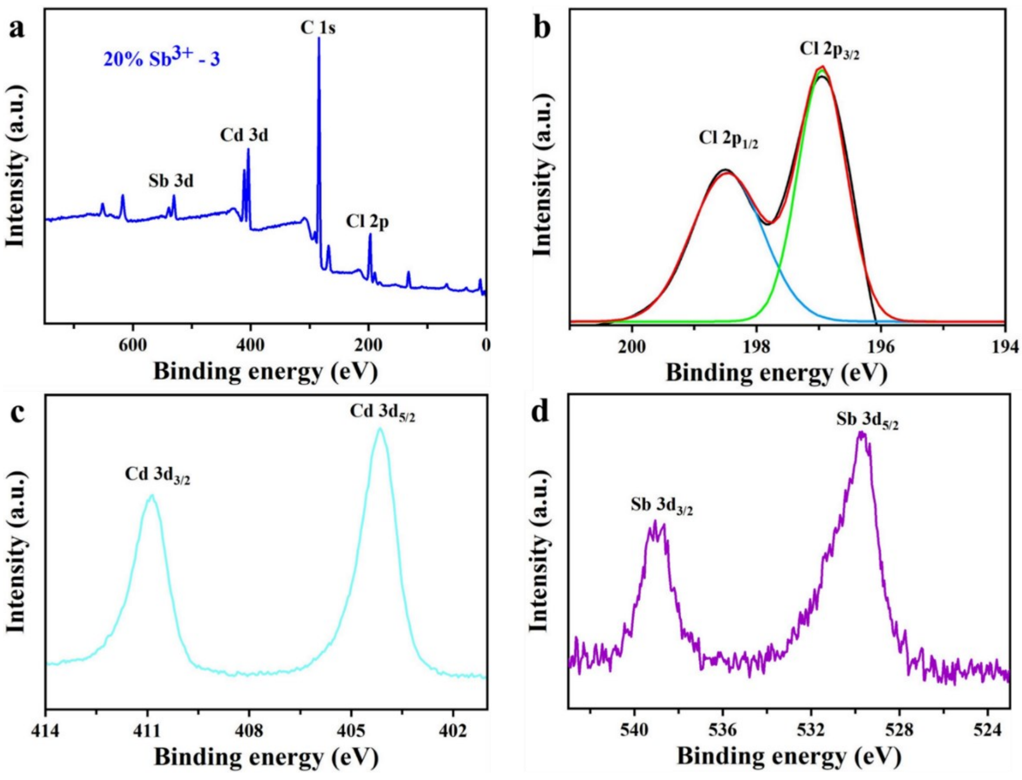

Figure S6. a) XPS spectrum of 20%Sb^{3+}-doped **3** and the corresponding high-resolution XPS spectra of b) Cl 2p, c) Cd 3d, d) and Sb 3d.

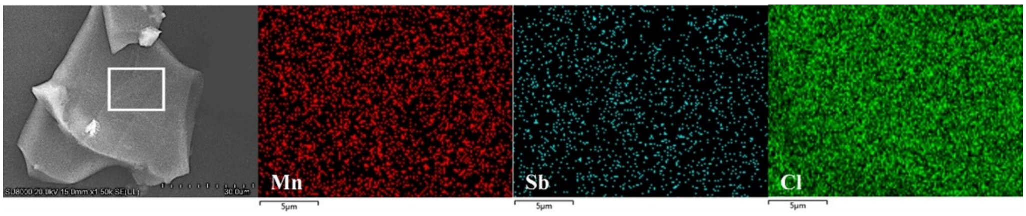

Figure S7. SEM image of 25%Sb^{3+}-doped **1** and the element mapping images of Mn, Sb, and Cl respectively.

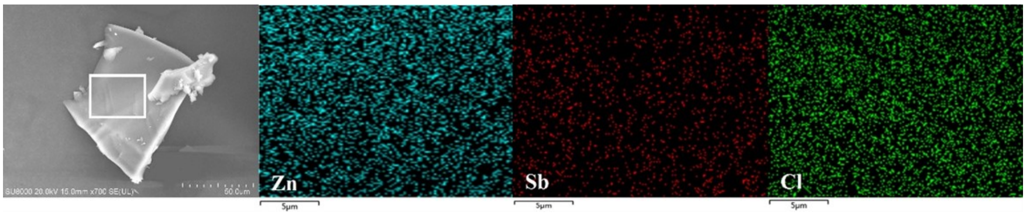

Figure S8. SEM image of 20%Sb^{3+}-doped **2** and the element mapping images of Zn, Sb, and Cl respectively.

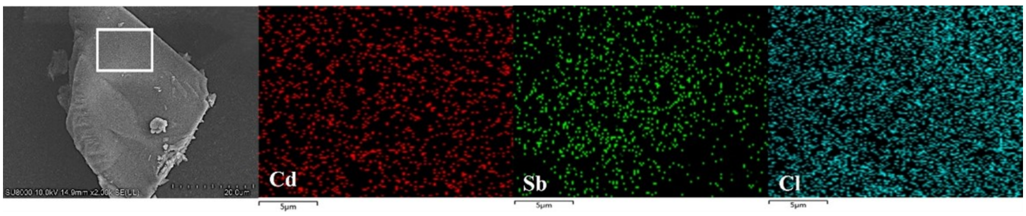

Figure S9. SEM image of 20%Sb^{3+}-doped **3** and the element mapping images of Cd, Sb, Cl respectively.

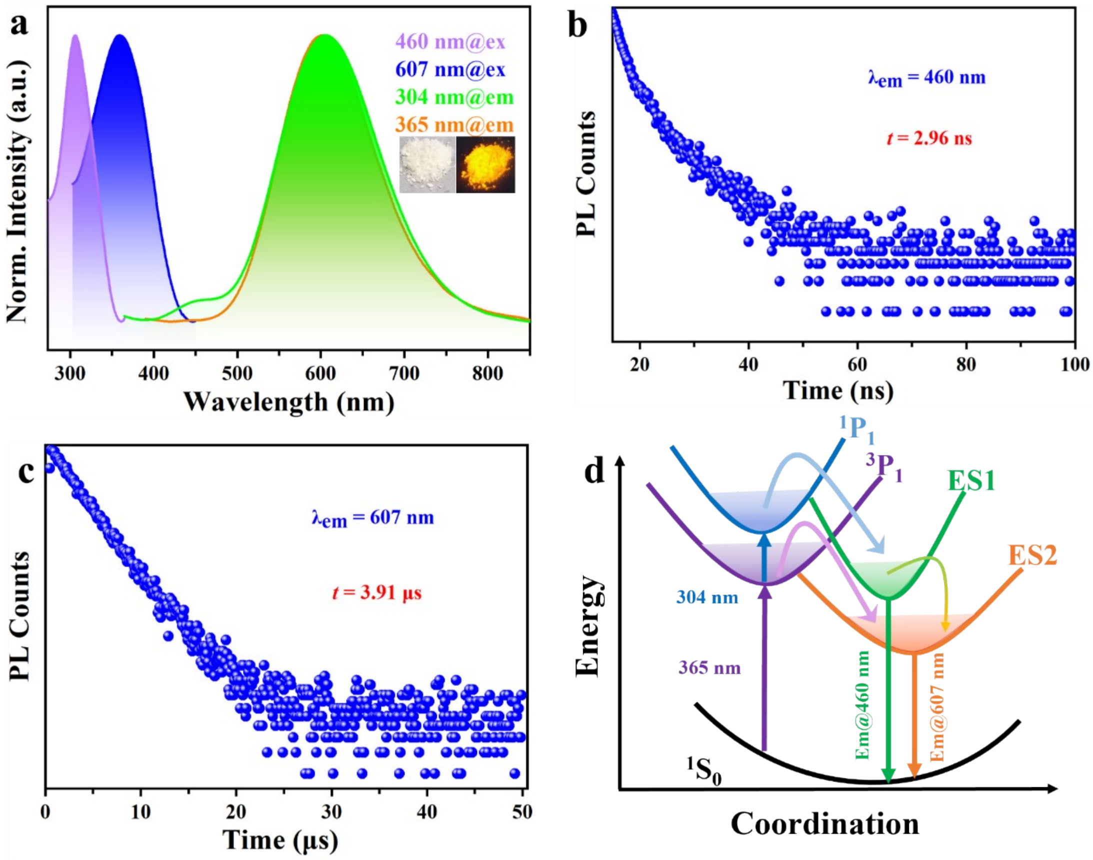

Figure S10. a) PLE and PL spectra of $(C_{20}H_{20}P)_2SbCl_5·EtOH$. PL decay lifetimes of $(C_{20}H_{20}P)_2SbCl_5·EtOH$ monitored at b) 460 nm, c) and 607 nm. d) Possible photophysical processes of $(C_{20}H_{20}P)_2SbCl_5·EtOH$.

Note：The possible photophysical processes of $(C_{20}H_{20}P)_2SbCl_5·EtOH$ can be summarized as follow:

For Sb^{3+} with $5s^2$ electron configuration, the ground state (GS) is called $^1S_0$, while the excited state split into four energy levels, namely, $^1P_1$ and ^3P_n (n = 0, 1, 2). The transitions $^1S_0 \rightarrow ^3P_0$ or $^1S_0 \rightarrow ^3P_2$ are forbidden, and the transitions of $^1S_0 \rightarrow ^3P_1$ or $^1S_0 \rightarrow ^1P_1$ are parity-allowed owing to spin-orbit coupling.[1-3] Owing to the large separation of $^3P_1$ and $^1P_1$, they can both couple with different multi-phonons to form different STEs, i.e., singlet and triplet STEs in $[SbCl_5]^{2-}$ units (Figure S9d). Therefore, the possible photophysical process of pure Sb (III)-based compound can summarized as follow: Upon HE photoexcitation (e.g., 304 nm), electrons are excited to the high-energy excited states of $^3P_1$ and $^1P_1$ states. Then, the excited electrons are rapidly transferred into LE excited states ES1 and ES2 via intersystem crossing, and then return to ground state of $^1S_0$. Finally, the narrow HE emission band (460 nm) and broad LE emission band (607 nm) can be obtained via the radiative recombination from singlet and triplet STEs in $[SbCl_5]^{2-}$ units. More particularly, only a single broad emission band at 607 nm with a lager stokes shift can be obtained under LE irradiation (e.g., 365 nm), which is derived from the triplet STE emission.

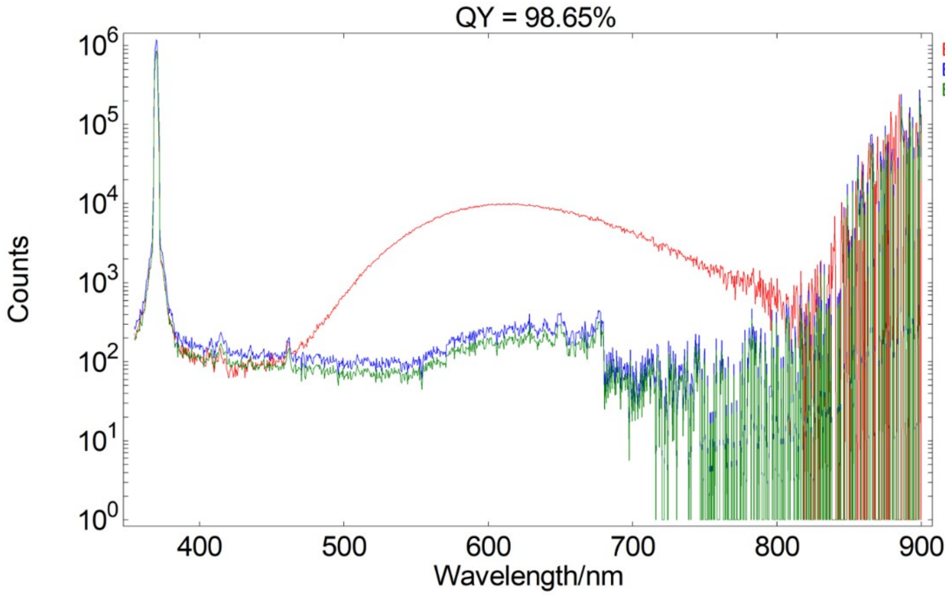

Figure S11. PLQY of $(C_{20}H_{20}P)_2SbCl_5 \cdot EtOH$.

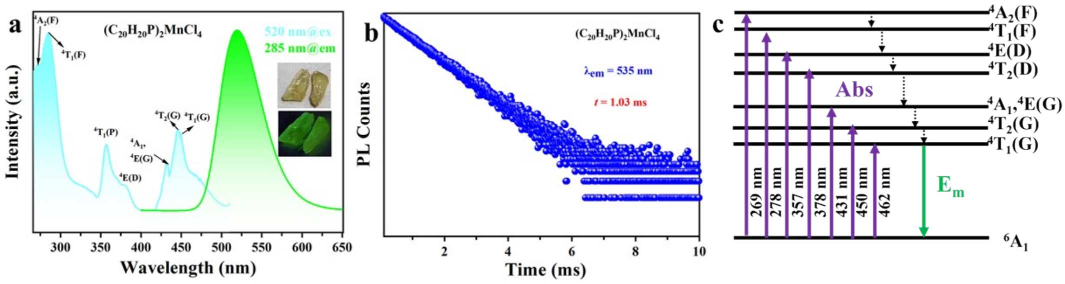

Figure S12. (a) PLE and PL spectra of $(C_{20}H_{20}P)_2MnCl_4$. (b) PL decay lifetimes of $(C_{20}H_{20}P)_2MnCl_4$. (c) Schematic diagram of the energy absorption, non-radiative relaxation, and emission processes in $(C_{20}H_{20}P)_2MnCl_4$.

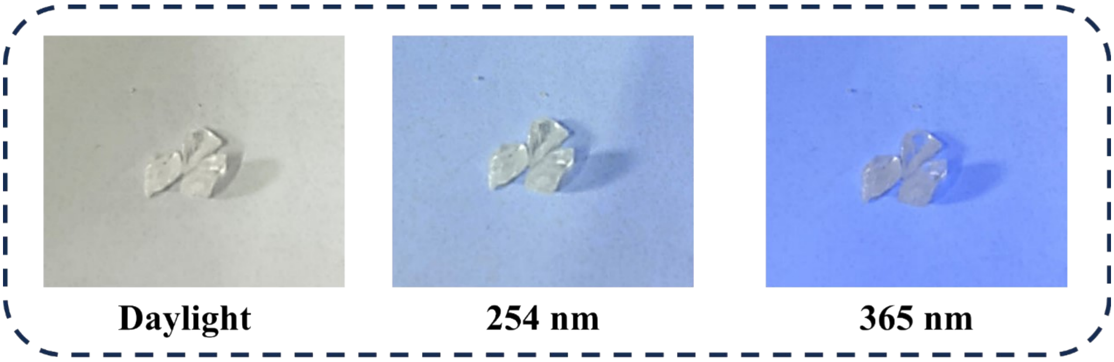

Figure S13. Optical images of Compound **2**.

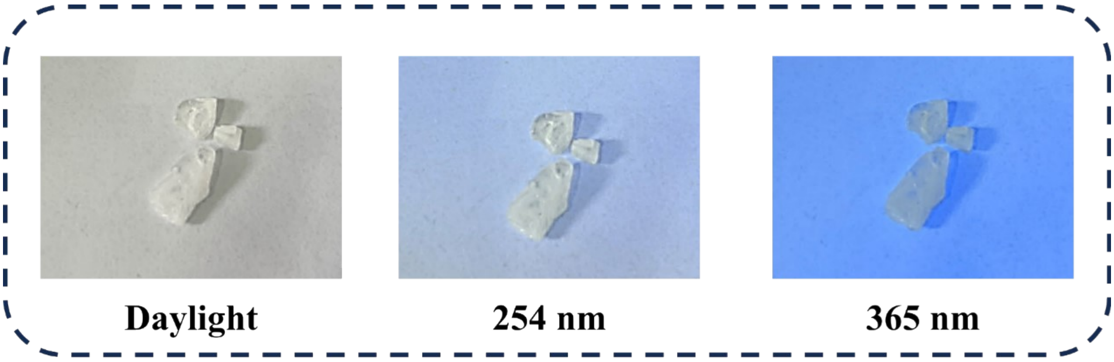

Figure S14. Optical images of Compound **3**.

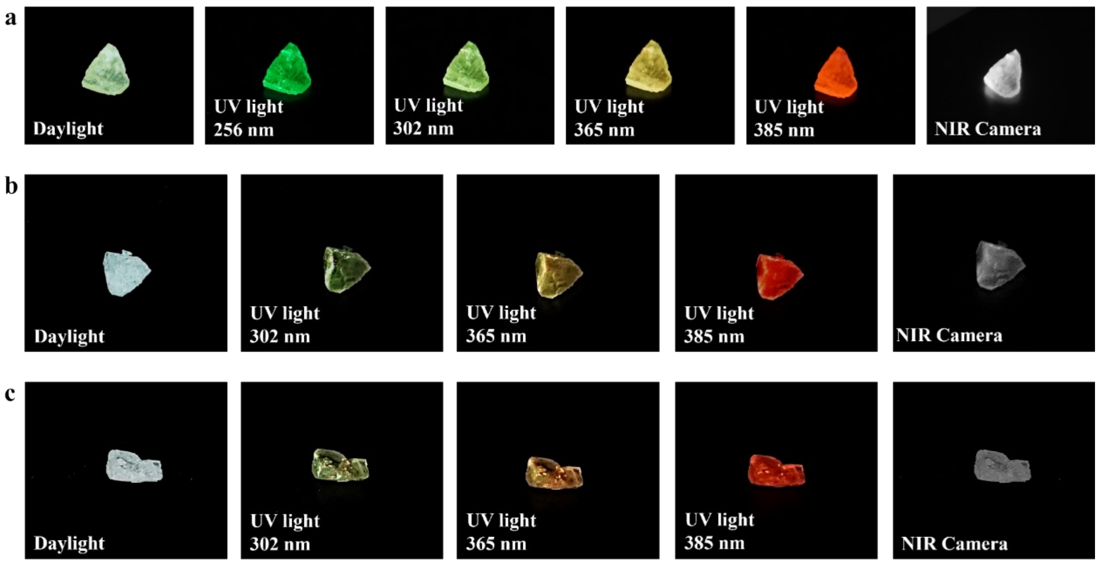

Figure S15. Optical images of a) 25%Sb^{3+}-doped **1**, b) 20%Sb^{3+}-doped **2**, and c) 20%Sb^{3+}-doped **3** single crystals.

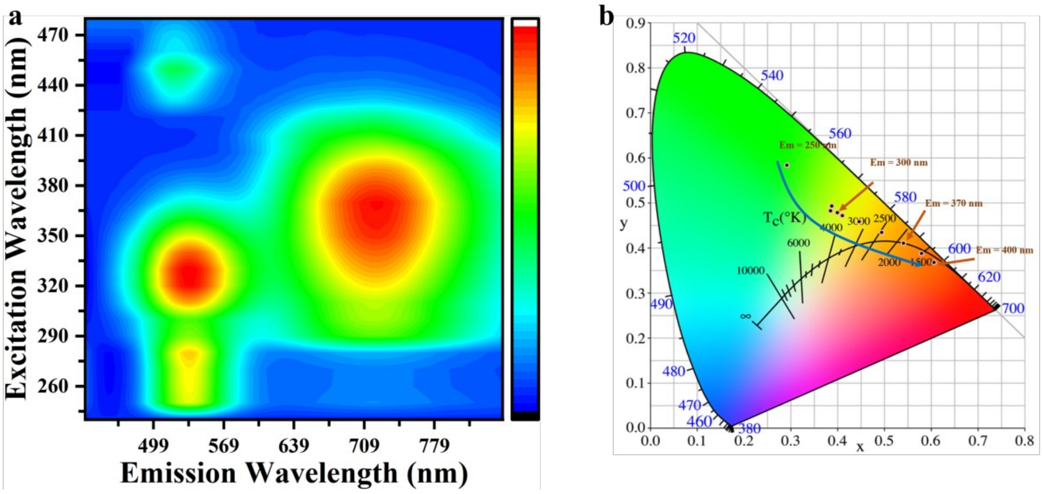

Figure S16. a) Emission spectra of 25%Sb^{3+}-doped **1** under different excitation wavelengths. b) CIE coordinates of 25%Sb^{3+}-doped **1** under different excitation wavelengths.

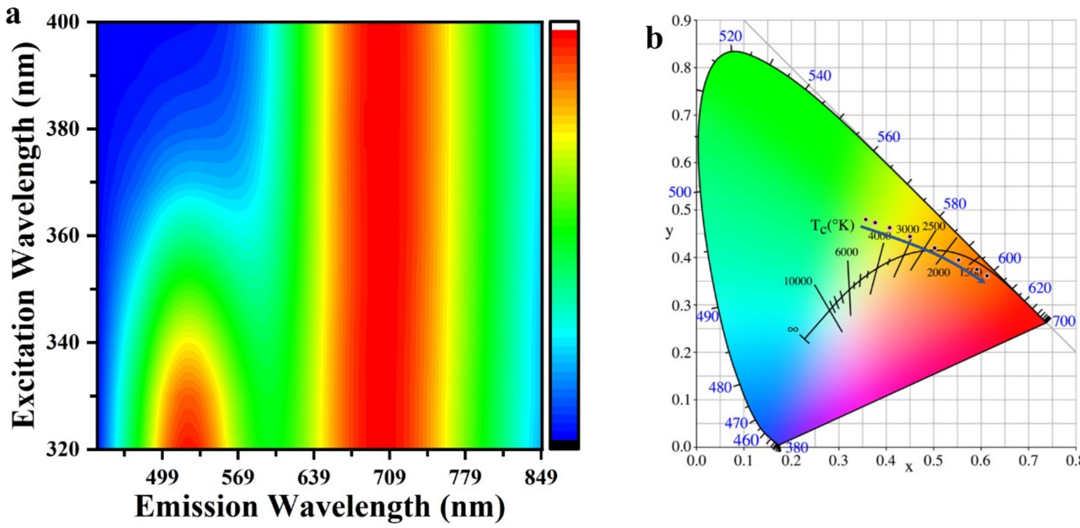

Figure S17. a) Emission spectra of 20%Sb^{3+}-doped **2** under different excitation wavelengths. b) CIE coordinates of 20%Sb^{3+}-doped **2** under different excitation wavelengths.

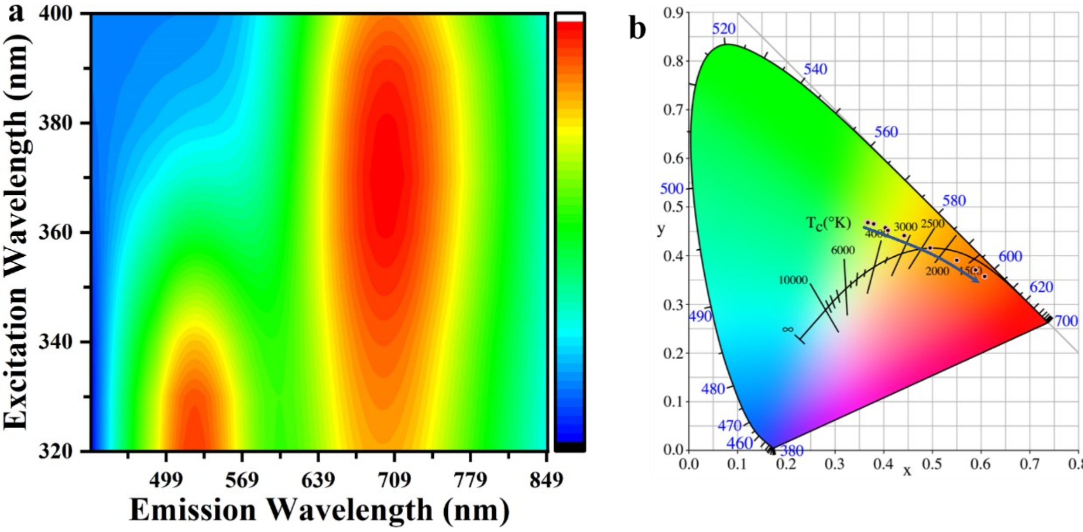

Figure S18. a) Emission spectra of 20%Sb^{3+}-doped **3** under different excitation wavelengths. b) CIE coordinates of 20%Sb^{3+}-doped **3** under different excitation wavelengths.

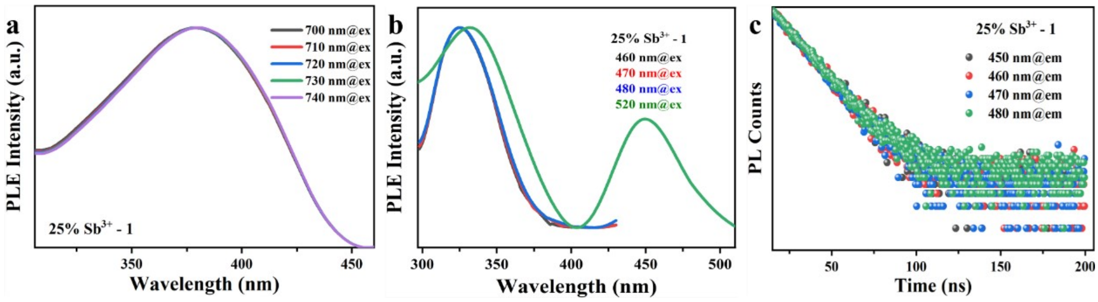

Figure S19. a) Excitation spectra of 25%Sb^{3+}-doped **1** monitored at 700-740 nm emission wavelengths, b) and 460-520 nm emission wavelengths. c) PL decay lifetimes of 25%Sb^{3+}-doped **1** monitored at 450-480 nm emission wavelengths.

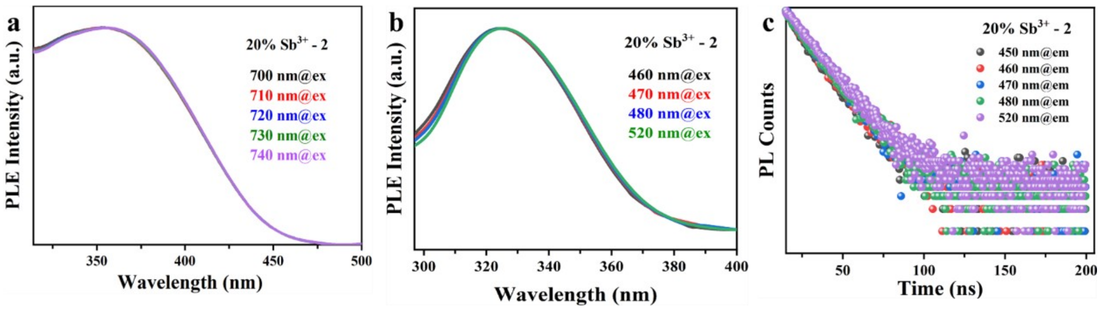

Figure S20. a) Excitation spectra of 20%Sb^{3+}-doped **2** monitored at 700-740 nm emission wavelengths, b) and 460-520 nm emission wavelengths. c) PL decay lifetimes of 20%Sb^{3+}-doped **2** monitored at 460-520 nm emission wavelengths.

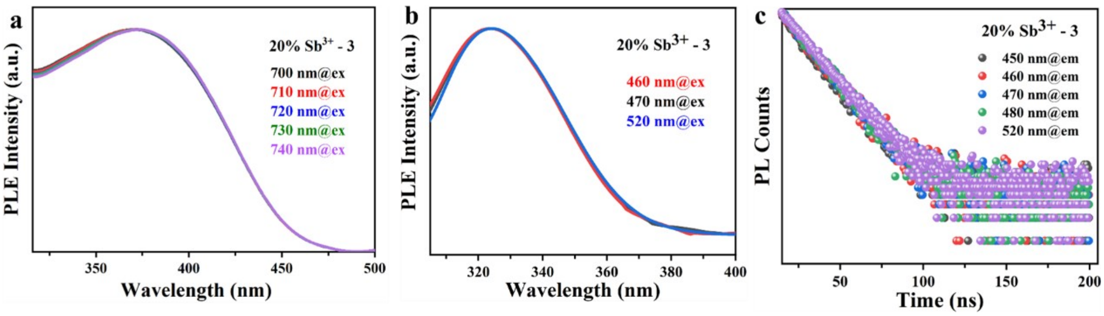

Figure S21. a) Excitation spectra of 20%Sb^{3+}-doped **3** monitored at 700-740 nm emission wavelengths, b) and 460-520 nm emission wavelengths. c) PL decay lifetimes of 20%Sb^{3+}-doped **3** monitored at 460-520 nm emission wavelengths.

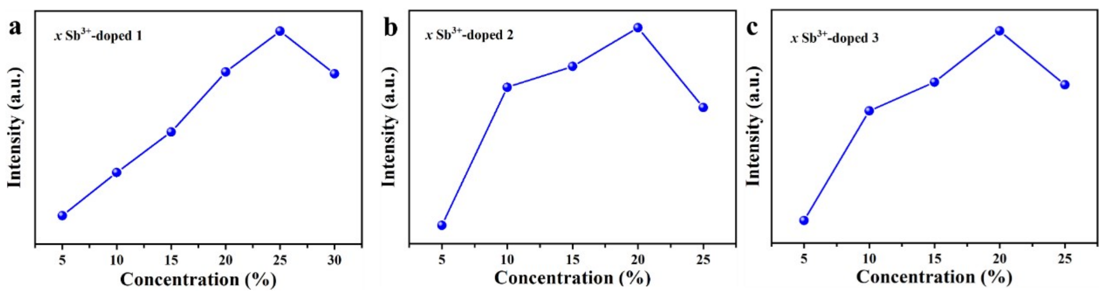

Figure S22. Emission intensity of a) x%Sb^{3+}-doped **1**, b) x%Sb^{3+}-doped **2**, c) and x%Sb^{3+}-doped **3** under different Sb^{3+}-doping concentrations.

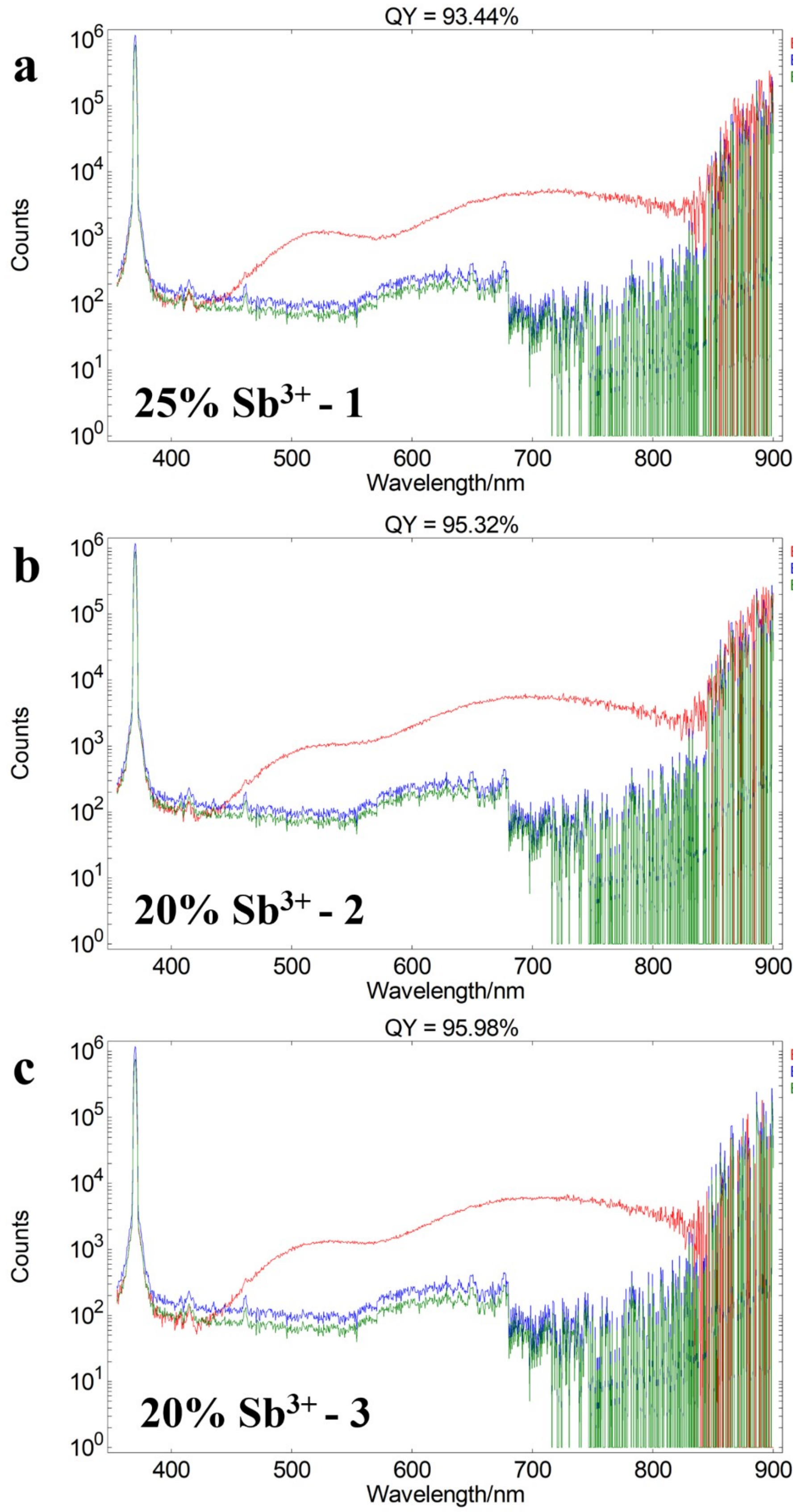

Figure S23. PLQY of a) 25%Sb^{3+}-doped **1**, b) 20%Sb^{3+}-doped **2**, c) and 20%Sb^{3+}-doped **3**.

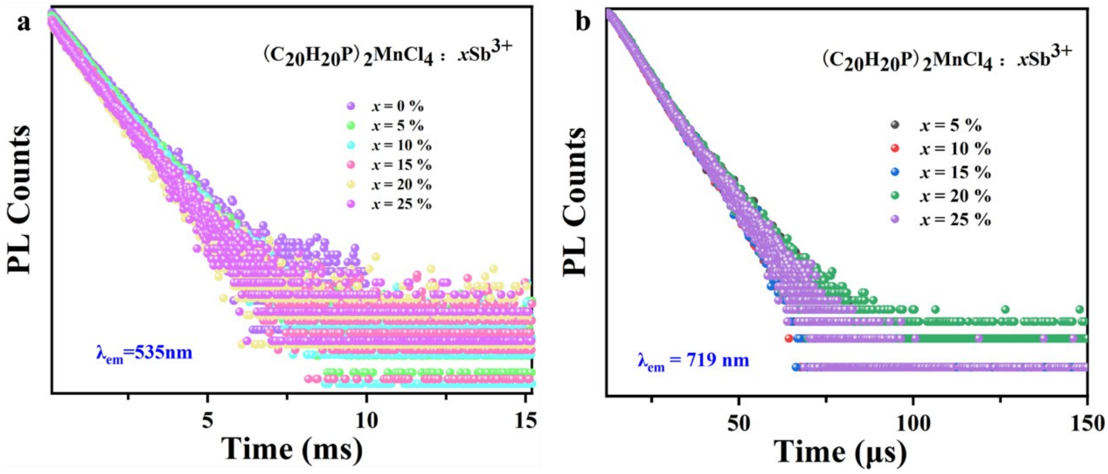

Figure S24. PL decay lifetimes of x%**Sb^{3+}-1** monitored at a) 535 nm, b) and 719 nm, respectively.

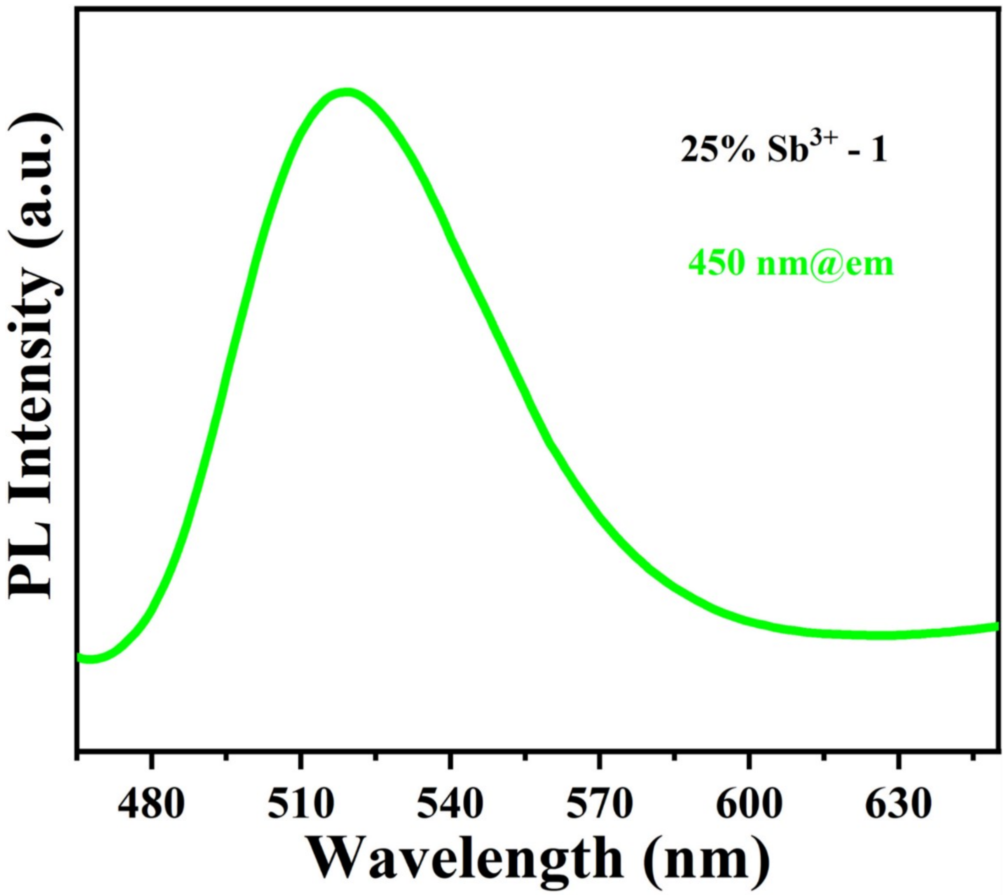

Figure S25. Emission spectra of 25%Sb^{3+}-doped **1** under 450 nm excitation.

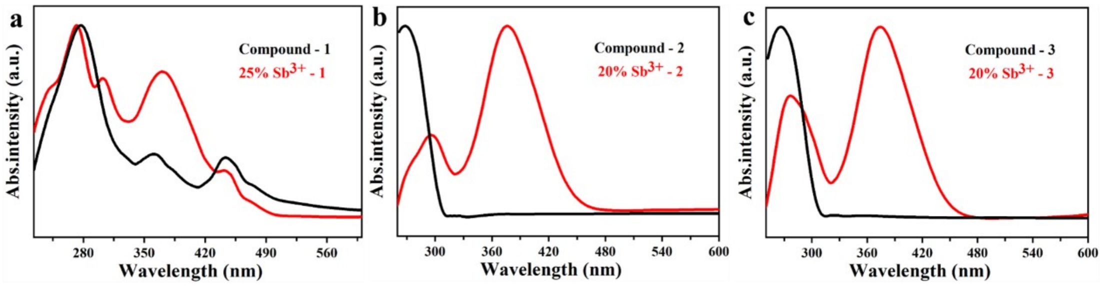

Figure S26. Absorption spectra of a) compound **1**, 25%Sb^{3+}-doped **1**, b) compound **2**, 20%Sb^{3+}-doped **2,** c) and compound **3**, 20%Sb^{3+}-doped **3**.

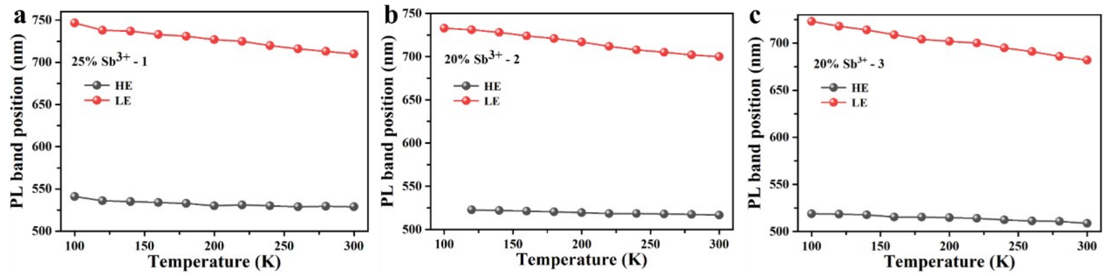

Figure 27. Temperature-dependent HE and LE band positions of a) 25%Sb^{3+}-**1**, b) 20%Sb^{3+}-**2**, c) and 20%Sb^{3+}-**3**, respectively.

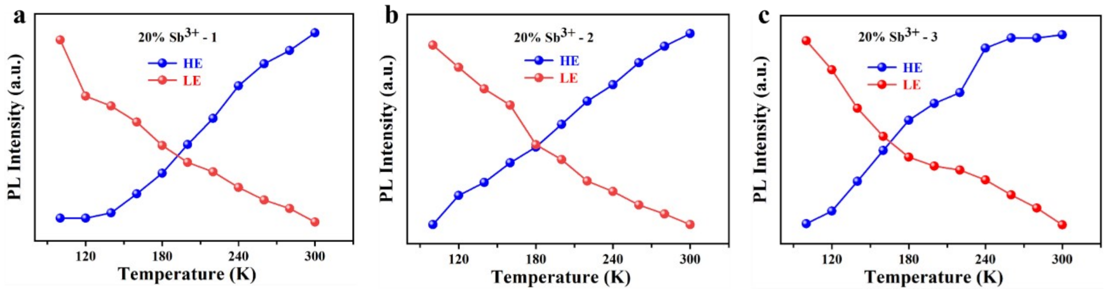

Figure 28. Temperature-dependent HE and LE band emission intensity of a) 25%Sb^{3+}-**1**, b) 20%Sb^{3+}-**2**, c) and 20%Sb^{3+}-**3**, respectively.

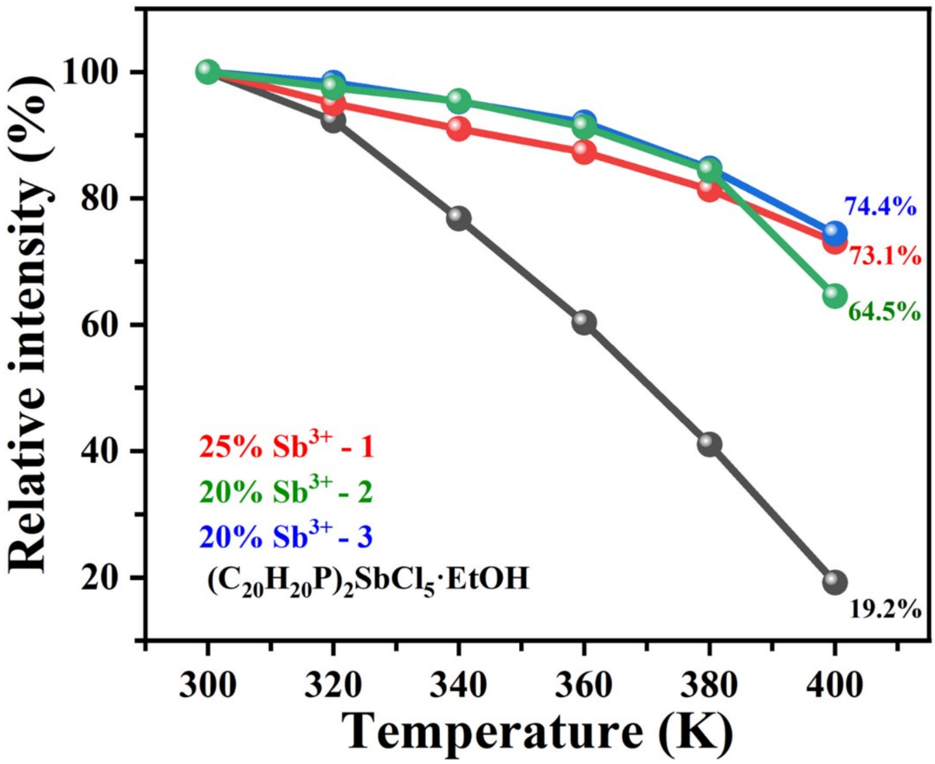

Figure S29. Temperature-dependent relative PL intensities of $(C_{20}H_{20}P)_2SbCl_5{\cdot}EtOH$, 25%$Sb^{3+}$-doped **1**, 20%$Sb^{3+}$-doped **2**, and 20%$Sb^{3+}$-doped **3** under high temperature.

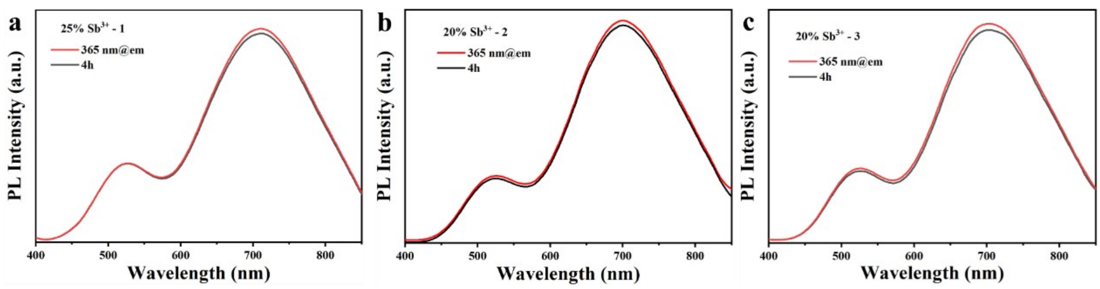

Figure S30. PL intensity of a) 25%Sb^{3+}-doped **1**, b) 20%Sb^{3+}-doped **2**, c) and 20%Sb^{3+}-doped **3** under 365 nm UV lamp irradiation for 4 hours.

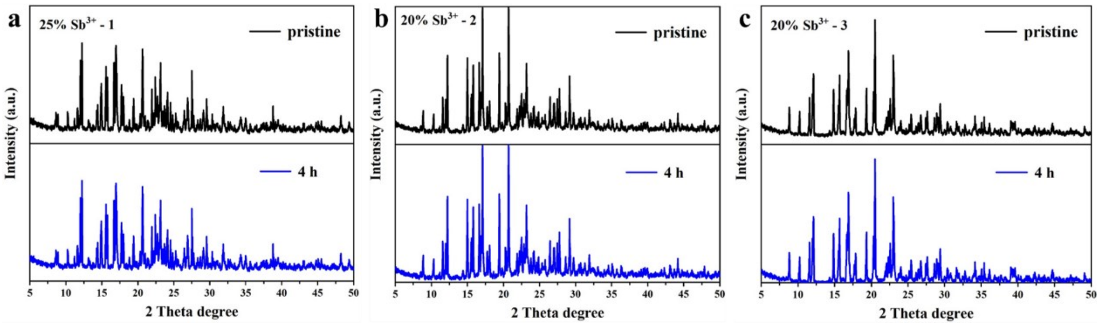

Figure S31. PXRD patterns of a) 25%Sb^{3+}-doped **1**, b) 20%Sb^{3+}-doped **2**, c) and 20%Sb^{3+}-doped **3** under 365 nm UV lamp irradiation for 4 hours.

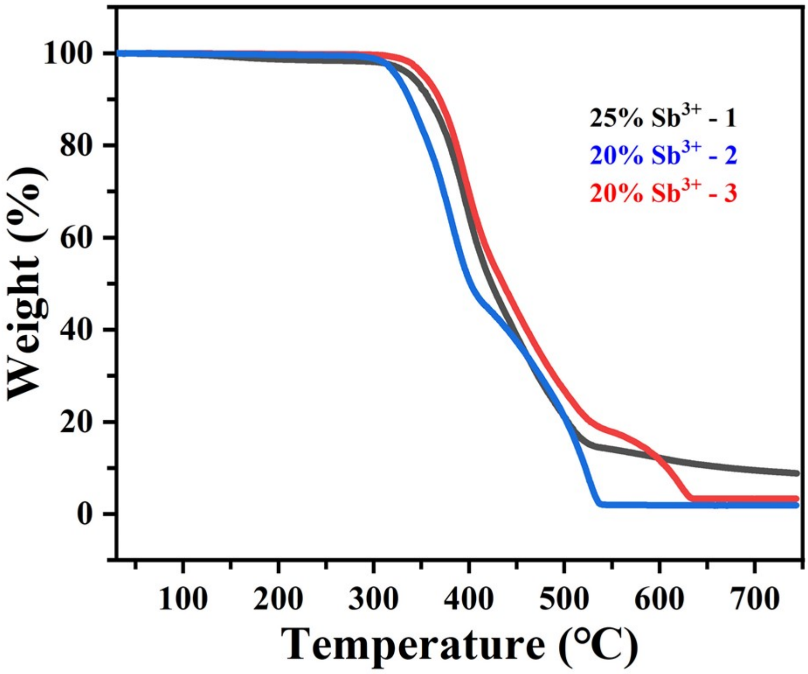

Figure S32. TGA curves of 25%Sb^{3+}-**1**, 20%Sb^{3+}-**2**, and 20%Sb^{3+}-**3**.

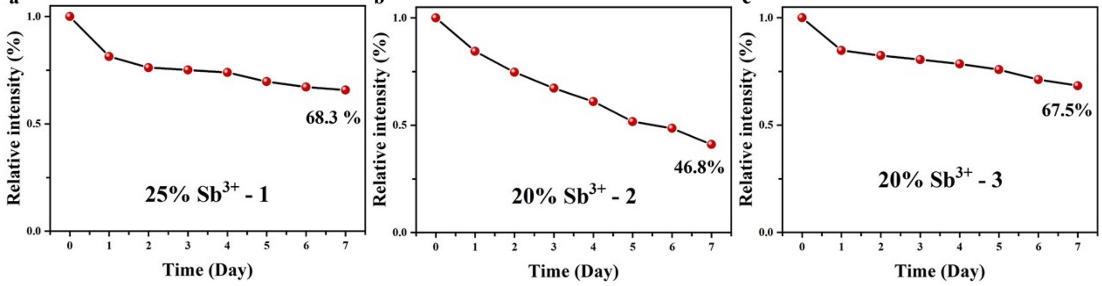

Figure S33. The commercial aging stability (humidity: 85%, temperature: 85 °C) of a) 25%Sb^{3+}-doped **1**, b) 20%Sb^{3+}-doped **2**, c) 20%Sb^{3+}-doped **3**.

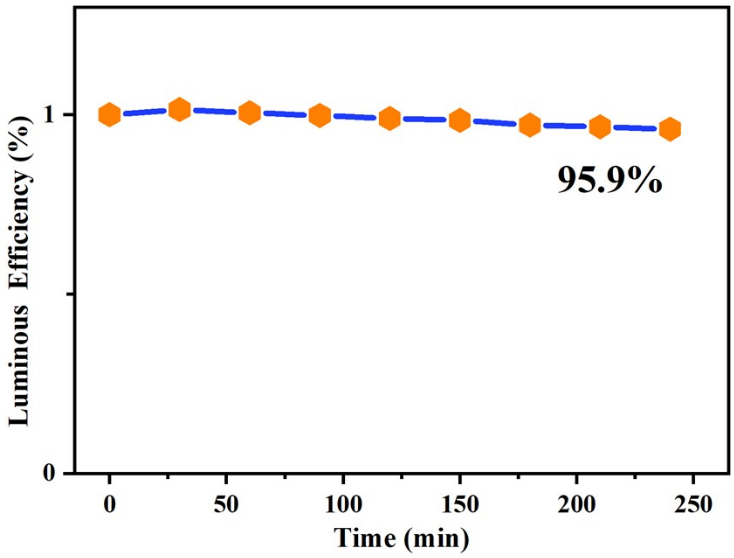

Figure S34. Operational stability of the 25%Sb^{3+}-doped **1** based NIR pc-LED.

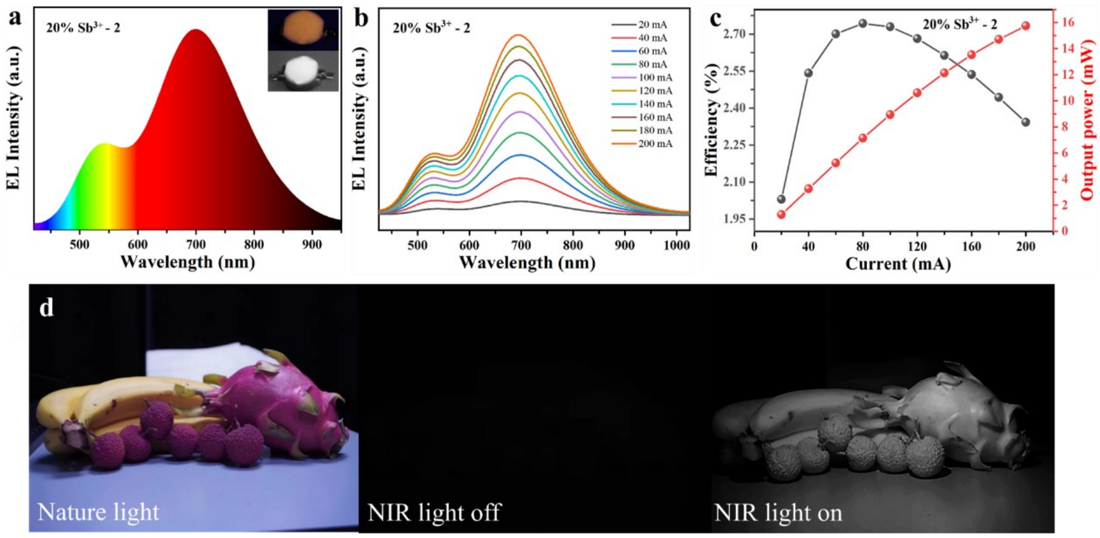

Figure 35. a) EL spectrum of 20%Sb^{3+}-doped **2** under 20 mA drive current. The inset shows the optical image of as-fabricated NIR pc-LEDs taken by a visible camera (top) and a NIR (bottom) camera, respectively. b) Driven current-dependent EL spectra of the NIR pc-LED. c) Photoelectric conversion efficiency and output optical power under various drive currents of the as-fabricated device. d) Photographs of fruit under natural light (left), and NIR pc-LED is turned off (middle) and turned on (right) captured by visible camera and NIR camera, respectively.

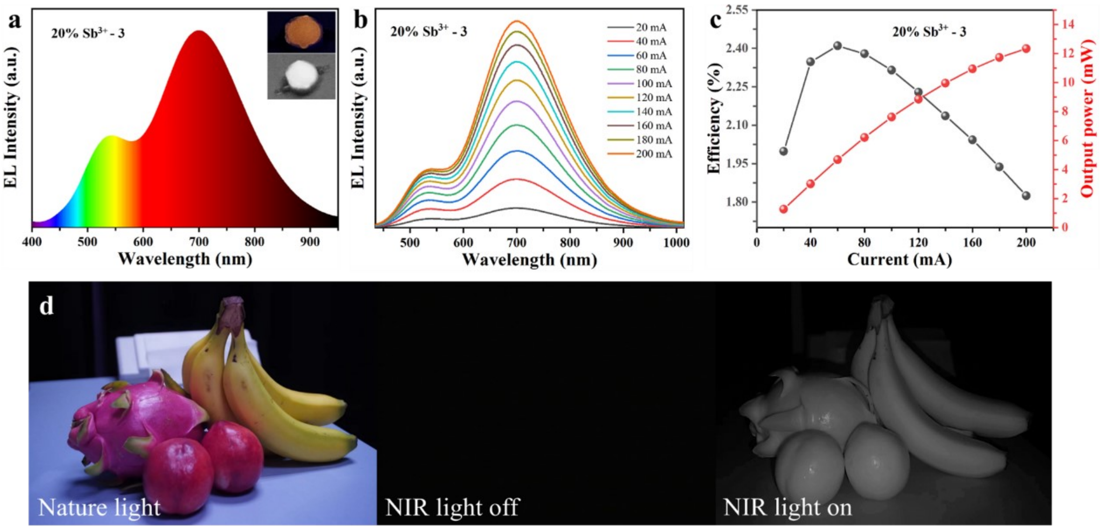

Figure 36. a) EL spectrum of 20%Sb^{3+}-doped **3** under 20 mA drive current. The inset shows the optical image of as-fabricated NIR pc-LEDs taken by a visible camera (top) and a NIR (bottom) camera, respectively. b) Driven current-dependent EL spectra of the NIR pc-LED. c) Photoelectric conversion efficiency and output optical power under various drive currents of the as-fabricated device. d) Photographs of fruit under natural light (left), and NIR pc-LED is turned off (middle) and turned on (right) captured by visible camera and NIR camera, respectively.

References

[1] Z. Z. Zhang, J. C. Jin, L. K. Gong, Y. R. Lin, K. Z. Du, X. Y. Huang, *Dalton Trans.* **2021**, *50*, 3586-3592.

[2] Y. Jing, Y. Liu, M. Li, Z. Xia, *Adv. Optical Mater.* **2021**, 9, 2002213.

[3] A. Biswas, R. Bakthavatsalam, B. P. Mali, V. Bahadur, C. Biswas, S. S. K. Raavi, R. G. Gonnade, J. Kundu, *J. Mater. Chem. C* **2021**, *9*, 348-358.